Check for updates

A clinical Raman spectroscopy imaging system and safety requirements for *in situ* intraoperative tissue characterization†

François Daoust, [ID] [a,b] Hugo Tavera, [ID] [a,b] Frédérick Dallaire, [ID] [a,b] Patrick Orsini,[c] Keven Savard,[c] Jacques Bismuth,[c] Philippe Mckoy,[c] Israel Veilleux,[a,b] Kevin Petrecca[d] and Frédéric Leblond*[a,b]

Raman spectroscopy imaging is a technique that can be adapted for intraoperative tissue characterization to be used for surgical guidance. Here we present a macroscopic line scanning Raman imaging system that has been modified to ensure suitability for intraoperative use. The imaging system has a field of view of $1 \times 1 \text{ cm}^2$ and acquires Raman fingerprint images of 40×42 pixels, typically in less than 5 minutes. The system is mounted on a mobile cart, it is equiped with a passive support arm and possesses a removable and sterilizable probe muzzle. The results of a proof of concept study are presented in porcine adipose and muscle tissue. Supervised machine learning models (support vector machines and random forests) were trained and they were tested on a holdout dataset consisting of 7 Raman images (10 080 spectra) acquired in different animal tissues. This led to a detection accuracy >96% and prediction confidence maps providing a quantitative detection assessment for tissue border visualization. Further testing was accomplished on a dataset acquired with the imaging probe's contact muzzle and tailored classification models showed robust classifications capabilities with specificity, sensitivity and accuracy all surpassing 95% with a support vector machine classifier. Finally, laser safety, biosafety and sterilization of the system was assest. The safety assessment showed that the system's laser can be operated safely according to the American National Standards Institute's standard for maximum permissible exposures for eyes and skin. It was further shown that during tissue interrogation, the temperature-history in cumulative equivalent minutes at 43 °C (CEM43 °C) never exceeded a safe threshold of 5 min.

Introduction

Cancer resection surgery is a frontline treatment during which surgeons identify bulk tumours visually and by palpation. Frozen section analyses and medical imaging modalities - e.g., magnetic resonance imaging (MRI)– can help to more precisely characterize the extent of cancer spread, oftentimes associated with pathological manifestations that are visually imperceptible. Although emerging techniques such as intraoperative MRI (iMRI) led to significant advances in surgical oncology, they

aDepartment of Engineering Physics, Polytechnique Montréal, 2500 chemin de Polytechnique, Montréal, QC H3T 1J4, Canada. E-mail: frederic.leblond@polymtl.ca
bCentre de recherche du Centre Hospitalier de l'Université de Montréal, 900 rue St-Denis, H2X 0A9 QC, Canada
cOptech, 1111 Rue Lapierre, H8N 2J4 QC, Canada
dMontreal Neurological Institute-Hospital – McGill University, 3801 University Street, H3A 2B4 QC, Canada
†Electronic supplementary information (ESI) available. See DOI: https://doi.org/10.1039/d2an01946a

are not readily accessible in hospitals, mainly due to their high cost and the increased surgery time associated with their use. Moreover, iMRI can be limited in its ability to detect subtle biomolecular and morphological alterations associated with oncogenic processes initiated close to the borders of a tumour, thereby limiting the surgeon's capacity to maximize the volume of resected cancer.[1,2] On the other hand, pathology analysis of frozen sections is commonly used but they require on average 20 minutes, which can limit the frequency of their use during a procedure.[3,4] Failing to locate and completely remove tumours often result in follow-up repeat surgery from disease recurrence with concomitant negative impact on patient outcomes.

Amongst technologies that aim to guide surgeons in locating the full extent of cancer *live* during surgery is Raman spectroscopy. Label-free spontaneous Raman spectroscopy can reveal biomolecular information in the form of a tissue spectral fingerprint. That fingerprint can be matched with a known reference set by histology using machine learning methods, resulting in predictive mathematical models.[5,6] Several

in-human studies were conducted using this technology to characterize tumour tissue in breast,[7] brain,[8–10] colon,[11] skin[12–14] and prostate.[15,16] Raman-based systems could be available for surgical guidance in hospitals within the next decade.[17]

Although intraoperative Raman spectroscopy was mainly developed for millimetre-scale single-point detection, some reports point towards larger field-of-view Raman imaging at mesoscopic scales as a promising surgical guidance modality. This technique would have all the advantages of single-point Raman spectroscopy, albeit with the added benefit of providing molecular information over a larger surface area.[18,19] Large-area Raman spectroscopy could improve *in situ* biomolecular characterization of subtle oncogenic processes at the interface between cancer and normal tissue, providing surgeons with the ability to more accurately identify and visualize diffuse tumour borders.[20,21] For example, these technologies could help solve crucial clinical problems, including the detection of cancer infiltrations during glioblastoma surgery[22] and the detection of microscopic ductal carcinoma *in situ* (DCIS) lesions during breast conservation surgery.[23] Research laboratories have developed label-free large field of view Raman imaging systems for intraoperative surgical margin assessment in skin[24] and oral cancer.[25] Important limitations of these systems were their inability to achieve intraoperative measurements over a large field-of-view within in a timeframe minimizing disruption of the surgical workflow.

Our group previously developed a large-angle handheld Raman imaging line-scanning system.[26] The device could image over a field-of-view of 1 cm^2 at a spatial resolution of 0.25 millimeters (pixel size). Briefly, it had a light detection branch composed of a spectrophotometer, a charged-coupled device (CCD) camera and a galvanometer coupled to custom optics to detect over a line scanned over a specimen. Line excitation was achieved with a 785 nm laser based on custom optics and a translation stage to allow surface scanning. The excitation and detection lines were spatially co-located. The system also included a brightfield white-light source and standard red-green-blue (RGB) camera to allow video-rate widefield visualization of the specimen. Device performance was preliminarily demonstrated on animal tissue (porcine) and a machine learning data pipeline was developed to detect a tissue margin modelled by high adipose (fat) and high-protein tissue (muscle).

The system lacked several key features making it unsuitable for intraoperative use. Limitations included: the absence of a sterilization procedure, prohibitively long acquisition times in biological tissue and bulkiness resulting in lack of mobility. Further, the imaging probe could not be manoeuvred in space because of its weight and the lack of a flexible holding arm. Several safety considerations were also not addressed, including laser exposure limits and biocompatibility. Moreover, the imaging system was used to produce classification models trained and validated on only a limited number of porcine samples (3 samples), which prevented testing on an independent hold-out data subset.

In this paper we present an upgraded Raman imaging instrument suitable for intraoperative use. The system was modified to ensure patient and user safety, portability and probe head 3-D manoeuvrability, as well as tissue imaging times compatible with clinical use (<5 minutes per image). A crucial improvement was the development of a contact measurement sterilizable sub-unit (muzzle) flattening the interrogated tissue surface to ensure optimal positioning at the focal plane. Another key system upgrade was the integration a 3D-articulated arm and custom supporting the imaging probe. The new system was tested by acquiring a large dataset of porcine tissue images (21 samples) from which classification models were trained and evaluated using an independent hold-out testing set.

Experimental

Clinical prototype Raman imaging system

The system achieved line scanning over a field of view of 1 cm^2, allowing acquisition of Raman spectra over the spectral range 400–2100 cm^{-1} with a spectral resolution of 8 cm^{-1} (Fig. 1). Spatially collocated bright field images (*i.e.*, white light images) with a spatial resolution of 50 μm can be acquired to guide where Raman imaging is performed based on visually identifiable tissue landmarks. Laser line excitation at 785 nm and bright field illumination are relayed through an imaging fibre optics bundle (Schott, USA) to an imaging probe head. The images are relayed to the system's cameras through a second flexible imaging bundle. The use of imaging bundles enables the user to manoeuvre the probe at the desired location, alleviating the need for moving parts in the probe head itself. Line scanning is achieved using cylindrical lenses transforming the laser beam into a line followed by transmission into the excitation imaging bundle. A translation stage controls which area of the imaging bundle is illuminated
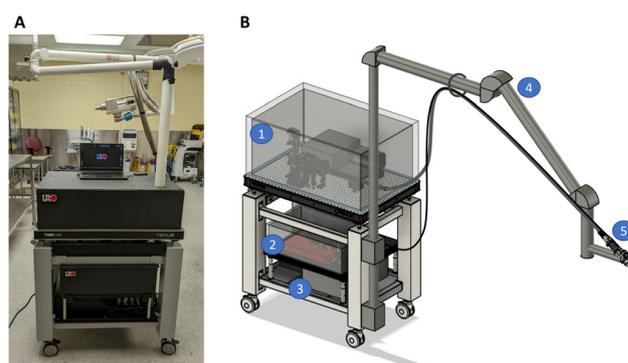
Fig. 1 (A) Cart-mounted clinical prototype of a Raman imaging system designed for intraoperative clinical measurements with (B) the computer aided design of the imaging system illustrating the location of several parts: (1) the collection branch covered by a light tight enclosure, (2) the excitation branch covered by its light tight enclosure, (3) the medical isolation transformer, (4) the articulated arm and (5) the imaging probe with its contact measurement muzzle.

while the detection bundle and the imaging probe optics relay the light reemitted following line excitation to a spectrophotometer. The on-sample excitation line dimension is 400 μm × 10 mm. The Raman collection line dimension is 200 μm × 10 mm and its on-sample location is collocated with the excitation line using a mirror mounted on a galvanometer (Novanta Photonics, USA) placed in the optical path leading to the spectrophotometer.

Optical design changes were made to improve performance of the system compared with our group's prior version. First, the system's spectrophotometer was replaced by a custom-designed spectrograph (slit width: 1 cm, NA 0.22; EH 0001 model, EmVision, USA) with an entrance slit of 200 μm (previously 75 μm) which increased light throughput by a factor of 2.7 with minimum impact on the spectral resolution (8 cm^{-1} instead of 6 cm^{-1}). A second design change consisted of using a more powerful 785 nm multimode laser (5 W instead of 1.8 W, Innovative Photonic Solutions, USA) with a lower numerical aperture (NA 0.39 instead of NA 0.5). Finally, the lens responsible for focusing the light reemitted from the sample onto the new spectrometer was changed for optimal etendue matching based on ray tracing simulations (OpticStudio®, Zemax, USA). This increased light detection efficiency by 42% at the centre of the image and by 26% closer to its borders.

In addition to the previously mentioned upgrades, several features were added to the Raman imaging system to make it suitable for use in an operating room. The prototype was mounted on a compact breadboard cart (POC001, Thorlabs, USA) to ensure mobility. Light tight enclosures made of black cardboard (TB4, Thorlabs, USA) were used for the light collection and excitation sub-units, preventing laser light from inadvertently endangering staff while keeping any ambient light from contaminating the collected signal. A medical-grade isolation transformer (MEDBOX-1200, Amgis LLC, USA) was installed to protect the system and the users from electrical power surges and faulty components. An articulated support arm (BRAPT7880, B&D, Italy) was also integrated into the system with the purpose of maintaining the imaging probe in place. This articulated arm extended over 1.5 m to keep the imaging system body out of the way of clinical staff and, when applicable, away from the sterile field (e.g., for use in neurosurgery). The arm also allowed the user to position the probe close to the patient and to hold it in place during a measurement. The articulated arm had the added benefit of supporting the fibre optics bundles along its frame to reduce strain. Two draped lead bricks (18 kg each) were added as counterweights to prevent the system from tipping over when the articulated arm is fully extended. A custom probe mount was designed to secure the imaging probe to the articulating arm while allowing fine angle and position adjustments. This custom mount includes a manual translation stage with 8 cm travel distance for the probe head.

Two probe muzzles were designed that can be connected to the imaging probe using spring plungers. One muzzle was designed to allow contact measurements and one for non-contact measurements. The working distance of the non-contact measurements muzzle is 40 mm. Both muzzle units were made of sterilizable and biocompatible materials since they can come in direct contact with a patient. They were composed of three different parts: a main body, an optical window, an adhesive to keep the two pieces attached to one another. The probe muzzle body was made of 304 stainless steel which is commonly used for clinical applications due to its resistance to corrosion, its biocompatibility, and its tolerance to most sterilization methods. The front window of the probe muzzle was either made of an MgF_2 or CaF_2 Raman grade optical window (Crystran, United Kingdom). These materials have low inelastic scattering signal (from 400 to 2100 cm^{-1}) and low fluorescence signal when excited at 785 nm. Finally, the adhesive used to attach the optical window to the probe muzzle body consisted of a high temperature resistant (up to 350 °C) epoxy (EPO-TEK® 353ND) designed for fibre optics and medical applications. The epoxy was cured at 160 °C for 1 hour. For future probe muzzles dedicated to intraoperative in situ imaging, a medical variant of this epoxy (EPO-TEK® MED-353ND: ISO 10993-tested, certified biocompatible) could be employed. All probe muzzle materials are known to be compatible with conventional sterilization cycles of autoclave steam, ETO gas, gamma radiation and vaporized hydrogen peroxide gas plasma. A sterilization procedure, shown in the ESI,† included sterilizing the probe muzzle and covering the imaging probe and articulated arm with a sterile surgical drape. Fig. 2 shows the imaging probe with the contact measurement muzzle mounted on the articulating arm.

The system was controlled via custom software developed using LabVIEW (National Instruments, USA). In case of emergency, a button was installed that allows the operator to immediately shutdown the laser.
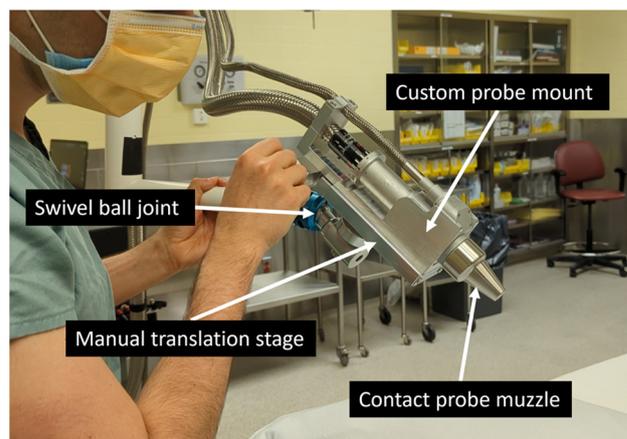
Fig. 2 Imaging probe with its attached probe muzzle for contact measurements, mounted on an articulated support arm allowing the user to move the probe with ease. A manual translation stage with 8 cm travel distance lets the user position the probe ensuring contact with the tissue area targeted for imaging.

Spectral data pre-processing

Cosmic rays were removed using a 2D median filter. Luminescence measured during an image acquisition in mid-air was subtracted from all raw spectra. This luminescence is additive in nature and mostly comes from the focusing achromatic triplet in the Raman imaging probe. Following this, spectral misregistration (also known as "smile")[27] correction and wavenumber calibration were applied based on a reference measurement of Acetaminophen powder. The spectral misregistration was corrected using 4 steps: (1) locate the pixel positions of the 12 most prominent Acetaminophen Raman peaks in the computed average of spectra from the centre of the CCD (corresponds to 40% of all spectra where wavelength shift is visually imperceptible), then for every spectrum in the Acetaminophen Raman image: (2) locate the pixel positions of the nearest corresponding peaks, (3) compute a second-degree polynomial fit, and, (4) apply a linear interpolation. Spectral misregistration correction resulted in a common wavenumber axis for all spectra within an image. The wavenumber calibration was completed using a cubic-spline interpolation based on the 5 prominent peaks (651.6, 857.9, 1168.5, 1323.9 and 1609.0 cm^{-1}) from the Acetaminophen Raman fingerprint spectrum. Relative intensity correction of each spectrum was achieved using a reference Raman image measurement on a NIST reference material (SRM 2241, NIST, USA). Artifacts that appeared on the reference measurement caused by scratches on the NIST material were filtered with a 2nd order 2D Gaussian filter. A novel baseline removal algorithm named *BubbleFill* was used to isolate the inelastic signature from other contributions to the signal.[28] The resulting Raman spectra were then processed using standard-normal-variate (SNV) normalization.

Imaging of biological tissue

The biological specimens in this study were porcine tissue from 3 different pigs, herein labelled pigs #1, #2 and #3. Specifically, 2 porcine loin samples were used per pig and each set of loins were purchased at different butcher shop. This choice was made for preliminary proof-of-principle studies because of accessibility, the well-established Raman signature of muscle and adipose tissue[29,30] as well as the visually apparent tissue borders between adipose and muscle tissue, used here as a toy model for tumour borders. Each pig sample was approximately 2 cm thick with a 10 cm diameter and was placed over black aluminium foil tape (T205-2.0, Thorlabs, USA) to minimize background luminescence from the sample support. The tissue was imaged using the parameters shown in Table 1. Three different areas per specimen were selected based on visual inspection: pure adipose, pure muscle and adipose-muscle tissue interface. In total, 21 images were acquired: 6 in adipose tissue, 6 in muscle tissue and 9 included an adipose-muscle tissue interface. In addition, 3 images were acquired using the contact measurements probe muzzle, one in pure adipose, one in pure muscle and one including a tissue interface. For each Raman image, a co-located bright field image was acquired.

Table 1 Raman imaging system parameters selected for the *ex vivo* tissue experiments

	Specifications
Field of view	1 cm^2
Working distance	40 mm (non-contact)
	0 mm (with contact muzzle)
Number of excitation lines	40 lines (10 mm × 400 µm each)
Distance between scanned excitation lines	250 µm
Pixel size	x-axis: 200 µm, y-axis: 250 µm
Spectral resolution NIR	8 cm^{-1} (at 1085 cm^{-1})
Number of pixels	x-axis: 40, y-axis: 42, λ-axis: 1024
Spectral range	λ-axis: 400–2100 cm^{-1}
Exposure time	7.5 seconds per line
	Total: 5 min in this study
Spatial resolution (field of view): bright field mode	50 µm (1 cm^2)

The imaging FOV of 1 cm^2 was covered by scanning 40 lines per image. Pixel binning along the spatial axis of the camera CCD (y-axis) was used to increase signal to noise ratio (SNR), which effectively increased the y-axis pixel size to 250 µm. The spatial offset between subsequent line measurements was 250 µm. The dimension of each Raman image was thus 40 (x-axis) × 42 (y-axis) × 1024 (wavenumber axis). Six columns of pixels on the image borders were always discarded due to low photon detection efficiency in those regions. This resulted in Raman images 36 × 40 spatial pixels, for a total of 1440 spectra. The laser line excitation profile was 400 µm × 10 mm with a total power of 905 mW corresponding to an average on-sample intensity of 22.6 W cm^{-2}. The luminescence (*i.e.*, Raman and background fluorescence resulting from 785 nm excitation) from 400 to 2100 cm^{-1} (810 to 940 nm) was collected for each line during a 7.5 s exposure time. Bright field images allowed placement of the sample surface at the focal plane of the system. The broadband source was turned off during line-scanning Raman spectroscopy imaging. Every measurement was conducted within a custom-designed light tight enclosure to prevent ambient light sources from contaminating spectroscopic signals.

Classification

Two classification algorithms, support vector machines (SVM) and random forests (RF), were investigated. The classifiers were trained, validated, and tested to perform pixel-wise classification (*i.e.*, no spatial features were used, only spectral features associated with Raman band intensities). Tissue labels were assigned visually to each imaged pixel using the collocated bright field images. The training set consisted of all 7 Raman images (10 080 spectra) from pig #1. The validation set consisted of all 7 images (or 10 080 spectra) from pig #2. Finally, the testing set consisted of the remaining 7 images (10 080 spectra) from pig #3. The training, validation and testing sets were independent from each other, and all contained 2 images of only muscle tissue, 2 images of only adipose tissue and 3 images containing adipose-muscle tissue interfaces. An additional testing set (4320 spectra) was

obtained from the 3 additional Raman images acquired in pig #3 with the contact measurement probe muzzle. This testing set consisted of one Raman image from a tissue interface, one image from adipose tissue and one image from muscle tissue.

The classification data pipeline consisted of manual feature selection followed by feature standardization and classifier development. Manual feature extraction (*i.e.*, handpicking of prominent Raman peaks following visual inspection of the spectra in the training set) took precedence over automated feature extraction (*e.g.*, principal component analysis [PCA]) since it lets human understanding of the discrimination task lead the selection of the features.

In total, 8 Raman features were manually selected for classification from the training dataset. The features selected had a visually apparent peak prominence for at least one tissue type and had a relevant biological assignment for its tissue type. For example, Raman features associated with lipid content were chosen as markers of adipose tissue and features associated with protein content as markers of muscle tissue. All selected features were for peaks with a Raman shift ≥ 1000 cm^{-1} due to lower SNR below that range. Both SVM and RF classifiers were trained on the training set from pig #1 using a grid search over optimization parameters (hyperparameters). Linear and Gaussian kernels were considered for SVM models where the regularization parameter C was varied between 0.001 and 1 and the kernel coefficient parameter γ was varied between 0.001 and 10. Random forest models were trained with either 100, 200, or 300 trees, each single tree being trained with maximum 60%, 70%, or 80% of the training samples. The combination of parameters produced a total of 24 SVM models and 9 RF models. These models were then used to predict adipose and muscle tissue spectra on the validation set (pig #2).

The RF and SVM models having the highest validation accuracy in pig #2 were tested on the independent datasets from pig #3 (*i.e.* 7 images acquired without a probe muzzle and 3 images acquired with the probe muzzle). Pixel-wise predictions were computed along with their corresponding probabilities and were shown next to their respective bright field images to allow visually interpretation of the classification results. Class probabilistic outputs were computed using Platt scaling, which effectively quantifies model prediction confidence.[31] Probability scores varied from 0.5 to 1.0 where 1.0 corresponded to the highest confident class membership probability. A value of 0.5 was the lowest class membership probability. Algorithms from the Python library Scikit-learn were used.[32]

Clinical safety assessment

The imaging probe muzzle serves as an intermediary between the probe body and the patient. Because the probe body will never be sterilized, there remains a risk of infection if there is not a proper seal between the probe muzzle window and the probe muzzle body. Three contact measurements probe muzzles were manufactured and their hermiticity was evaluated using a helium leak testing device (979 Helium Leak
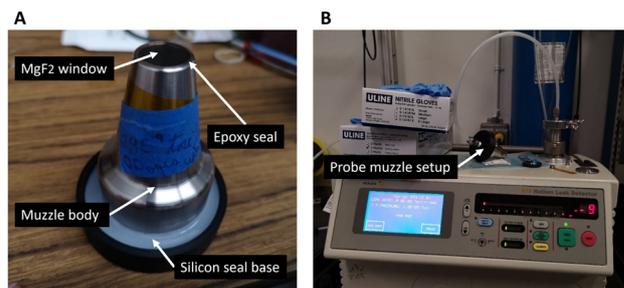
Fig. 3 (A) Contact measurements probe muzzle mounted on a hermetic silicon base for a helium leak test and (B) leak test setup using a helium leak detector.

Detector, Varian, USA) combined with a custom-made silicon base (Fig. 3). To test the probe muzzle resistance to heat such as in a steam autoclave, one probe muzzle (Serial 00002) underwent a dry and high temperature cycle: 22 °C–145 °C–22 °C with 1 °C incrementation and 60 min at peak temperature, and it's hermeticity was once again measured.

Laser exposure risk to the eyes was evaluated for the system's operator and the other operating room staff (*e.g.*, nurses, research staff and anaesthesiologists). With an output power of 0.905 W at 785 nm per line, the imaging system emits enough laser light to cause permanent damage to the retina. The beam intensity was computed for various distances from the probe tip and the maximum permissible exposure (MPE) for eyes was computed according to the Z136.1 ANSI Laser safety standard[33] using the equations shown in the ESI.† The maximum beam power was also experimentally measured at different distances from the imaging probe, using an optical power meter (PM100D, Thorlabs, USA) and a thermal power sensor (S425C, Thorlabs, USA) having a 2.54 cm diameter input aperture.

Accidental laser exposure risk to skin for operating staff and patients was evaluated using the MPE for skin from the ANSI Z136.1 standard. The risk involving a continuous wave near-infrared (NIR) laser consists of thermal effects to tissue (*e.g.*, coagulation, cauterizing and burning). Risk assessment was done near the area with the highest laser intensity during measurements, *i.e.*, at the imaging probe focal plane. The maximum power (per line) in this study was 0.905 W at 785 nm. The total output energy was computed for a total imaging time of 7.5 s averaged over a circular area of 3.5 mm diameter as per the ANSI Z136.1 standard's guidelines. Equations and detailed results for MPE in skin with the imaging system are shown in the ESI.†

Intentionally administered laser radiation for diagnostic applications may exceed the MPE if the risk is warranted according to ANSI Z136.3 laser safety in healthcare.[34] The MPE was therefore exceeded during Raman measurements. However, the thermal risk to interrogated tissue was assessed by measuring the temperature–time history of the tissue surface during laser exposure with the cumulative thermal dose CEM43 °C. The latter is an accepted metric for assessing

thermal dose and risk of thermal damage in tissues and is referenced to evaluate the safety of heat exposure in humans and animals in hyperthermia therapy,[35] radiotherapy,[36] and ultrasound.[37] CEM43 °C is computed using the measured time-dependant tissue temperature profile, *i.e.* $T(t)$,[38]

$$\text{CEM43} \, ^\circ\text{C} = \int_0^t R^{(43-T(t))} \mathrm{d}t \qquad (1)$$

where R is a coefficient with values $R(T < 43\ ^\circ\text{C}) = 1/4$ and $R(T \geq 43\ ^\circ\text{C}) = 1/2$. Tissue damage was never observed for CEM43 °C < 5 min in large animals (*i.e.*, cats, goats, dogs, pigs and humans). Lowest values for which damages were observed in large animals was in dog brain for CEM43 °C = 7.5 min[39] It was also reported that in magnetic resonance radiofrequency exposure, a CEM43 °C = 9 min appeared to be an acceptable thermal dose threshold for most patients.[40]

Here, three different biological samples were studied *ex vivo*. Specifically, temperature profiles (surface temperature) were measured for porcine adipose tissue, porcine muscle tissue, and 5 mL of rat blood. This was done using a thermal camera (E45 ThermaCAM, FLIR, USA) and continuous-wave laser exposition of 60 s exposure (785 nm, 0.905 W per line). To emulate a real-world clinical setting, the measured temperature difference was added to the known average basal body temperature in humans (*i.e.*, 36.9 °C) and the resulting temperature profile $T(t)$ was used to calculate the normalized thermal dose from eqn (1). The animal ethics protocol was approved by the Institutional Animal Care Committee of the *Centre de recherche du Centre hospitalier de l'Université de Montréal* in accordance with the Canadian Council on Animal Care guidelines.

Results

Raman tissue imaging

The dataset consisted of 21 images (30 240 spectra) from 3 pigs, containing images of adipose tissue, muscle tissue and the interface of these tissues. The bright field images and the corresponding labels are presented in Fig. 4. The total class distribution was balanced with 5011 spectra from adipose tissue and 5096 spectra from muscle tissue. The average Raman spectra, raw spectra and standard deviation for each class are presented in Fig. 5(A), showing visually distinguishable molecular contrast between adipose and muscle tissue. The prominent molecular contrast is due to the difference in relative concentrations of lipids and proteins. As observed in the variance from Fig. 5(A), for identical acquisition parameters, spectra from muscle tissue have a lower signal to noise ratio (SNR) than those of adipose tissue.

A second dataset consisting of 3 images (4320 spectra) from pig #3 contained one image from an adipose-muscle tissue interface, one image of adipose tissue and one image of muscle tissue, all acquired with the contact measurements muzzle. The average Raman spectra, raw spectra and standard deviation for adipose and muscle spectra acquired with the contact muzzle are shown in Fig. 5(B). Specific Raman band
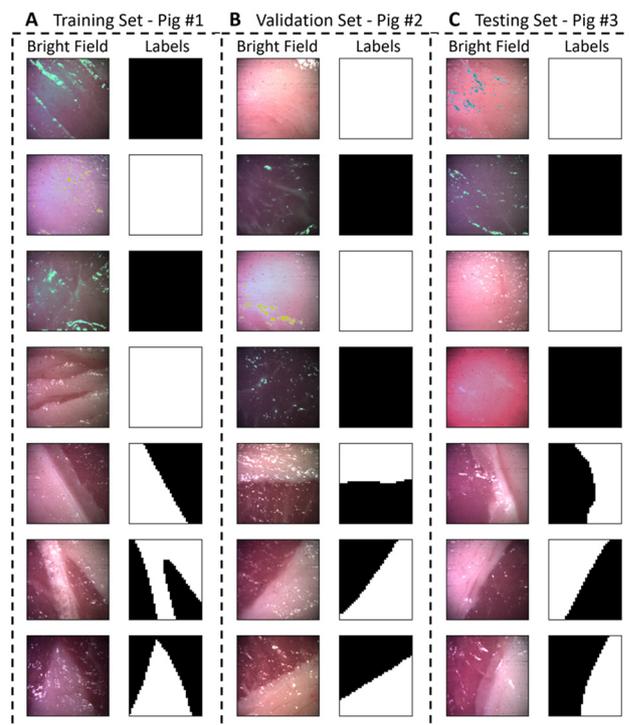

Fig. 4 Study non-contact dataset consisting of (A) the training set (7 measurements from pig #1), (B) the validation set (7 measurements from pig #2) and (C) the testing set (7 measurements from pig #3). For each subdivision of the data set, bright field images of porcine adipose and muscle tissue and their corresponding visually selected labels are shown. Black labels correspond to muscle tissue while white labels correspond to adipose tissue. Each square delimits a field of view of roughly 10 × 10 mm². In some bright field images, false colours including green tint were caused by an automatic white balance error introduced by the system's software.

assignments and biomolecular interpretation can be found in the ESI.†

Classification & tissue border detection

The SVM model with the highest validation accuracy had a Gaussian kernel with regularization parameter $C = 0.1$ and kernel coefficient $\gamma = 0.1$. The best performing RF model had 300 trees with each tree being trained with a maximum of 70% of all training instances. The best performing SVM and RF models had a training accuracy of 95% and 99%, respectively. Their validation accuracy was 98% for both SVM and RF. The features that were manually selected from the training set were the Raman peaks at 1004, 1062, 1265, 1295, 1340, 1459, 1652 and 1734 cm^{-1}.

Using the best trained/validated SVM model on the testing set resulted in prediction accuracy, specificity, and sensitivity of 96%, 94%, and 99%, respectively. Using the best trained RF model on the testing set resulted in prediction accuracy, specificity, and sensitivity of 96%, 95% and 98%, respectively.

Fig. 6 illustrates the first test set (*i.e.*, 7 Raman images acquired with no probe muzzle): bright field images, their corresponding labels, the pixel-based predictions, and their
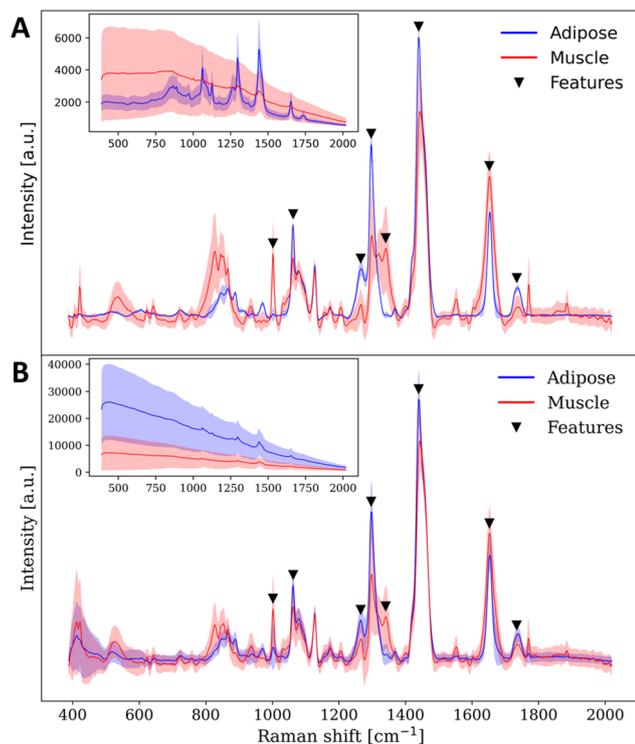
Fig. 5 Mean Raman spectra (solid line) and its 1x standard deviation (shaded area) for adipose (blue) and muscle (red) tissue of (A) the training dataset and (B) the contact muzzle testing set. For (A) and (B), the upper left spectra correspond to the mean raw luminescence counts and its 1x standard deviation for the same tissue types. Inverted black triangles correspond to the Raman features manually selected from the training data set for the classification.

respective probability assignments. A probability value of 1 (black) signifies absolute certainty of prediction while a value of 0.5 (white) signifies a random prediction. Classification on Raman images from the probe equipped with the contact muzzle resulted in prediction accuracy, specificity, and sensitivity of 97%, 98% and 97% when using the best SVM model and 94%, 100% and 89% when using the best RF model.

Clinical safety assessment

Leak tests from Table 2 show that the seal satisfies the 5×10^{-8} atm·cc s^{-1} rejection limit set by the Department of Defense Test Method Standard (MIL-STD-883E – Method 1014.10) which is referenced for medical applications. Following the dry and high temperature cycle: 22 °C–145 °C–22 °C, the measured leak rate of Serial 00002 was 1.32×10^{-9} atm·cc s^{-1}.

Results in Table 3 from calculated and measured laser intensities are showing which distances are safe to observe the tip of the probe for a duration exceeding 10 seconds with a maximum power output of 0.905 W. The laser beam exiting the imaging probe has a significant divergence created by the probes focussing lens. Optical simulations of the imaging system with OpticStudio® (Zemax, USA) have shown this beam has a rectangular shape and a divergence of 5.6° along the beam y-axis (10 mm) and 8.8° along the beam x-axis (400 μm).
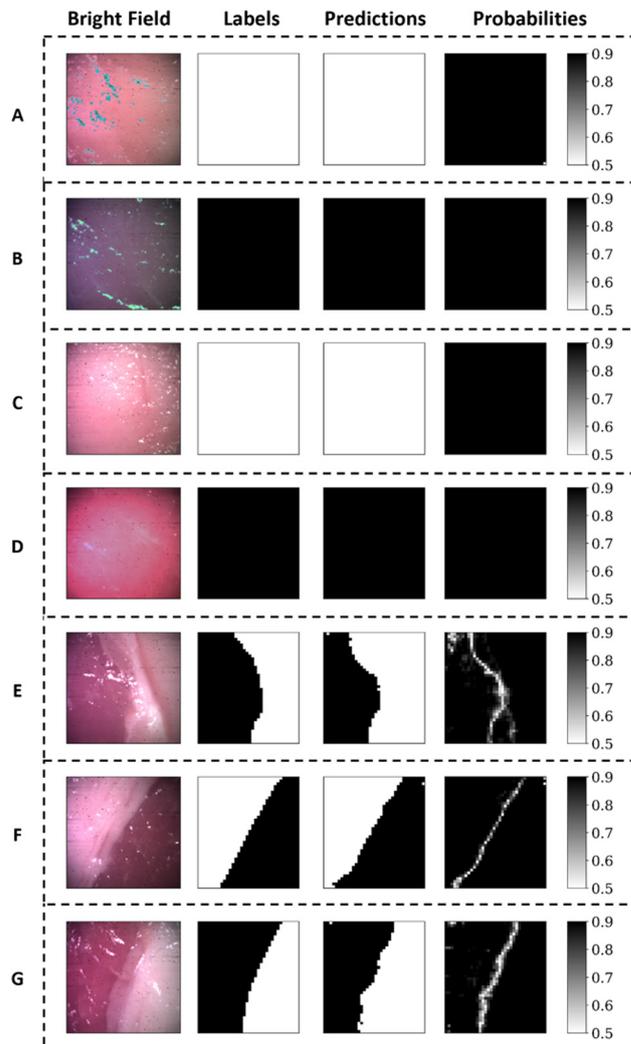
Fig. 6 (A–G) Raman images from the non-contact testing set (pig #3) with, from left to right respectively, the bright field image of the interrogated tissue, its corresponding labels (white for adipose tissue and black for muscle tissue), the classification predictions from the best performing SVM model and the assigned prediction probability. A prediction probability of 0.9 (black) indicates near certain prediction while a probability of 0.5 (white) corresponds to random prediction.

Table 2 Helium leak test results validating muzzle hermiticity

Muzzle serial no.	Optical window material	Leak rate [atm cc s^{-1}]
00001	MgF$_2$	5.80×10^{-9}
00002	MgF$_2$	3.82×10^{-9}
00003	CaF$_2$	5.01×10^{-9}

Due to this large divergence the output laser beam rapidly loses intensity the further away the beam is from the focussing plane (i.e., 40 mm from the imaging probe or 0 mm from the contact muzzle tip).

Calculated and measured laser intensities, along with known laser beam divergence suggest that for an exposure time <10 s, the safe distance of exposure for eyes is ≥16 cm

Table 3 MPE for eyes calculated and measured according to distance from the probe nose tip for an exposure time >10 s

Distance from contact muzzle tip [cm]	Measured power [W]	Measured intensity [W cm^{-2}]	Computed intensity [W cm^{-2}]	Below MPE eyes for >10 s
0	0.905	2.26×10^{1}	2.26×10^{1}	No
7.7	0.878	1.7×10^{-1}	4.2×10^{-1}	No
23.2	0.359	7.09×10^{-2}	7.7×10^{-2}	Yes
65.2	0.046	9.1×10^{-3}	1.2×10^{-2}	Yes
90.7	0.030	5.9×10^{-3}	6.6×10^{-3}	Yes

from the contact muzzle tip or ≥20 cm from the imaging probe. For an accidental exposure time of <1 s, the safe distance of exposure for eyes becomes ≥11 cm from the muzzle tip and ≥15 cm from the imaging probe.

Results from Table 4 suggest that accidental laser exposure to skin over 0.4 s per line at the probe tip exceeds the MPE. MPE computations also suggest that accidental skin exposure ≥10 cm from the probe tip is well below the MPE. The thermal study showed that recorded temperature differences for laser exposure up to 60 seconds in muscle tissue and adipose tissue (Fig. 7) never exceeded 1.5 °C and 1.0 °C, respectively. Considering the maximum induced temperature difference

Table 4 Excitation line laser intensity at the tissue surface for different exposure times and a power of 0.9 W compared to the MPE of skin of 3.27 W cm^{-2}

Exposure time [s]	Intensity permitted [W cm^{-2}]	Below MPE skin
0.3	4.01	Yes
0.4	3.23	Yes
0.5	2.74	No
1	1.63	No
5	0.49	No
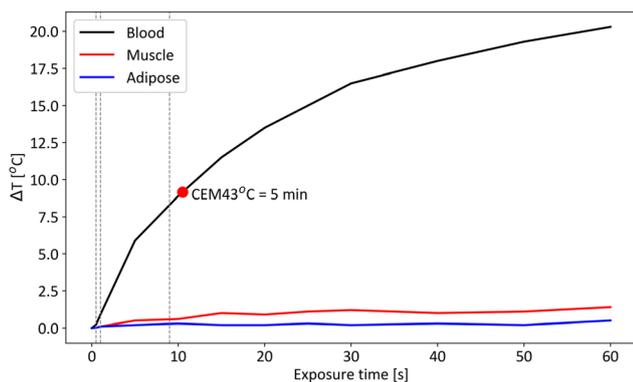
Fig. 7 Temperature difference following maximum laser exposure to blood (black), muscle (red) and adipose (blue) tissue for a total exposure time of 60 seconds. Each dotted line represents from left to right, 1×, 10× and 100× the skin MPE respectively. Only laser exposure to blood would exceed a safe limit of CEM43 °C = 5 min after an exposure time of 10.5 s if adding the recorded temperature difference to a basal body temperature of 36.9 °C.

(recorded during 60 s) in live animal or human tissue which would have an average basal temperature of 36.9 °C, this corresponds to a CEM43 °C = 1.7×10^{-3} min and 8.5×10^{-4} min for t = 1 min for muscle and adipose tissue respectively which in both cases are considered safe thermal doses. When exposing 5 mL of stagnant blood to the maximum laser exposure of the system, temperature differences significantly increased and CEM43 °C > 5 min occurred for an exposure time >10.5 s. For laser exposure time = 7.5 s in blood, CEM43 °C = 0.93 min which is well within a safe threshold of CEM43 °C = 5 min. Thermal doses evaluated in muscle tissue, adipose tissue and stagnant blood suggest the laser exposure parameters of the system (*i.e.*, 0.905 W power and 7.5 s per line exposure time) are safe for tissues.

Discussion

Raman imaging of biological tissue

One aspect of the work aimed at acquiring sufficiently large datasets to demonstrate the new Raman imaging device could be used towards the development of generalizable tissue classification machine learning models. This was achieved by creating a dataset from 6 porcine loin samples from 3 pigs for a total of 21 Raman and bright field images. Labelling of images proved challenging in some images where diffuse adipose tissue was observed. Without a more accurate method to precisely identify tissue lipid and protein content, (*e.g.*, histology) it is probable that some diffuse areas were mislabeled.

Discriminating adipose *versus* muscle tissue was used as a model for proof-of-principle studies although it bears limited clinical relevance to the intended use, *i.e.*, cancer detection. In fact, discriminating cancer from normal tissue typically results in spectral fingerprint differences more subtle than the changes detected between adipose and muscle tissue. However, the molecular content detected with Raman spectroscopy in those two tissue types cover all main peaks encountered in surgical applications, specifically Raman bands associated with lipids, proteins as well as aromatic amino acids.

Increase of background luminescence was observed when comparing contact with non-contact measurements acquired with the system. This was attributed to the highly fluorescent epoxy used to seal the probe muzzle. Although no fluorescence was observed when acquiring Raman images with the muzzle in mid-air, this epoxy was exposed to excitation light when acquiring measurements in a scattering medium. The system is then sensitive enough to collect the backscattered fluorescence generated in the epoxy. This added background signal did not impede tissue discrimination based on Raman spectra in adipose and muscle tissue. However, it is expected that for discrimination of tissues with much more subtle molecular differences such as normal *versus* cancer, the decrease in SNR may prevent accurate discrimination. For oncological applications, a change of epoxy in the probe muzzle is therefore warranted for contact measurements. Even so, when attempting to discriminate tissue types using Raman spectroscopy, we can circumvent

some signal differences introduced by environmental factors (*e.g.*, operating room lights) or by an apparatus, such as probe muzzle, by carefully selecting Raman features and classification parameters, as discussed below.

Classification and tissue border detection

As specified in the classification results, training accuracy for the best performing SVM and RF models reached 95% while validation accuracy exceeded 97%. The slightly lower training accuracy is attributed to Raman images in the training set containing some diffuse tissue borders and muscle tissue with high lipid content. Those may have been mislabeled or may present much more subtle molecular contrast not considered by the classifier. This did not prevent the trained model from discriminating adipose from muscle tissue with a high classification accuracy of 96% for both the SVM and RF models in an independent hold-out testing set.

Additionally, the model performed well in identifying tissue borders through classification probability assignment in Fig. 6. In fact, all predictions were attributed a high prediction probability of success except for clearly defined lines delineating the border between the two classes of tissue. These delineations correspond quite well to the location of the tissue interface identified in the labelling. It is indeed expected that at a tissue interface, the signal recovered will originate from a mixture of both classes of tissue which will lead to a reduced prediction confidence. The clinical implication from these predictions along with prediction probability across the boundaries are significant since tumor boundaries may be well-defined (*e.g.*, benign tumors) or diffuse (*e.g.*, malignant tumors). With a well-trained classifier for tumor detection, well-defined boundaries will appear as only being a few pixels wide while diffuse tumor boundaries will appear as a gradient of prediction probability that can extend up to several millimeters. We can observe, from the bright field images and corresponding prediction probabilities of tissue borders in Fig. 6, that even in the trivial case of adipose *versus* muscle tissue, not all tissue boundaries are the same pixel width. As such, this study presents an example of how prediction probabilities in Raman imaging can show the general location of tissue boundaries but can also show the local invasiveness (*e.g.*, infiltrations of cancer cells) at tissue borders. Such information presented could indicate to surgeons if they are working with diffuse tumors or not. This could be used as an aid to decision when assessing how much tissue needs to be removed.

Contact measurements with the probe muzzle used as a second testing dataset did not result in a significant degradation of predictive accuracy for both the SVM and RF models (*i.e.* for SVM: 97% with muzzle *versus* 96% without muzzle and for RF: 94% with muzzle *vs.* 96% without muzzle). The feature selection of prominent and relevant Raman peaks was successful in creating classifiers that circumvented a large degradation of SNR, introduced by the probe muzzle, to discriminate tissues with large molecular contrasts (*i.e.*, adipose and muscle tissue). However, the same strategy may be employed

to circumvent a smaller instrument response introduced by an improved probe muzzle, in a discrimination task involving tissues with more subtle molecular differences (*e.g.* cancer *versus* normal).

Clinical safety assessment

The measured leak rate of the probe muzzle (serial 00002) following a dry and heat cycle was 1.32×10^{-9} atm·cc s^{-1}. This result showed no degradation of the seal and a leak rate that remained satisfactory according to the rejection limit in MIL-STD-883E – Method 1014.10. This small leak test study gives confidence in the method of assembly of the probe nose, its design and its hermiticity. In the aim of developing a commercial product, such hermiticity will need to be tested in dozens of manufactured copies of the probe muzzle.

Regarding laser exposure risk to eyes, the MPE calculations suggest that an accidental laser exposure from the imaging probe poses only a risk to individuals in proximity of the imaging probe (*i.e.*, the surgeon or any personnel handling the probe). An operator would need to directly observe the tip of the probe, at a distance below 20 cm, while the laser is activated at maximum power. In a clinical setting, this would be unlikely since Raman image measurements, with laser power activated, are to be initiated only when the probe is placed in contact with or near contact facing the surgical cavity. Standard operating procedures such as keeping the laser off using a turnkey during imaging probe setup and activating the laser only when system is in place and ready for acquisition would help mitigate this risk. Finally, there is always the option of providing laser safety goggles for surgeons during the use of such a device. We consider the risk for eye exposure to the patient to be negligeable since patients are completely covered by opaque surgical drapes during major surgical procedures while also being sedated.

According to Z136.1 ANSI laser safety standards, results from Table 4 suggest that an accidental exposure to skin in immediate proximity of the probe tip needs to be avoided. As with accidental eye exposure, standard operating procedures in an operating room and staff training would make such an accidental exposure highly unlikely.

As for intentional laser exposure to tissue, the MPE for skin was exceeded up to a factor of 18 in this study yet no tissue damage was observed in the form of tissue discoloration or tissue burning. The cumulative thermal dose CEM43 °C was used a metric for evaluating dangerous laser exposure to tissues in a clinical setting. Temperature differences observed in Fig. 7 over a 60 s laser exposure would not expose live muscle or adipose tissue to a thermal dose exceeding CEM43 °C = 5 min. This assessment has its limits since live tissue will have circulation of whole blood which has an absorption coefficient μ_a = 0.34–0.54 mm^{-1} at 785 nm.[41] This absorption will increase temperature locally and increase the thermal dose on the interrogated area. Laser exposure to stagnant rat blood showed a difference of temperature that would exceed CEM43 °C > 5 min following ≥11 s of laser exposure from the system if added to the average basal temperature of

36.9 °C of mammals. Knowing that blood circulates through live tissue and dissipates heat, laser exposure to stagnant blood presents a worse-case scenario for a temperature increase following laser exposure at 785 nm. We add that anaesthesia of patients during surgical procedures usually causes a decrease in body temperature (<36.0 °C).[42] The permissible thermal dose through laser exposure with the system would therefore be greater during surgical procedures. With these results, it is expected that in live tissues during surgery, temperature differences and total heat exposure to tissue following the system's laser exposure will be between what was observed in adipose/muscle tissue and stagnant blood.

We conclude that, in accordance with the literature, we can safely and intentionally exceed the MPE for skin set by the ANSI standard by a factor of 10.5 s/0.4 s = 26 when performing Raman imaging with this system in live tissue. We are further confident with this assessment since our experiment was conducted in a worse-case scenario due to the absence of blood flow in the interrogated blood sample of this study, as opposed to live tissue, where heat transfer occurs by convection from blood perfusion.[43] Additionally, a cooling effect from cold air blown onto the tissue could help control local temperature increase such as in some laser therapies in skin.[44] The observed temperature differences observed are therefore much higher than one would expect in an *in vivo* setting. When intentionally exceeding the ANSI MPE for skin in a clinical setting, we recommend monitoring the surface temperature to assess and ensure that heat generated by laser exposure to tissues never exceeds known safe CEM43 °C.

Conclusions

This report presents an upgraded large field of view macroscopic line-scan Raman imaging system which has been modified into a clinical prototype ready for intraoperative tissue imaging. A dataset of bright field and Raman images was generated from porcine tissue allowing for the training, validation, and testing of robust classifiers. Clear contrast was observed in the spectra acquired in adipose and muscle tissue. Additionally, similar molecular contrast was present between adipose and muscle tissue imaged with and without the system's contact muzzle, which suggests a classification model could be generalizable to both cases. Biologically relevant Raman features were selected from the training set for classification of adipose and muscle tissue in porcine loins. SVM and RF classifiers were trained and validated, and the best performing SVM and RF models produced classification accuracies >94% on two separate independent testing sets of porcine loins (contact and non-contact measurements). Finally, safety assessments were conducted for biosafety and laser safety. It was shown that the sterilizable probe muzzle poses minimal biosafety risk to patients for intraoperative use while the system's laser can be used safely when observing standard operating procedures in the operating room while also respecting the CEM43 °C = 5 min thermal dose limit.

Author contributions

François Daoust: conceptualization, methodology, software, validation, formal analysis, investigation, resources, data curation, writing – original draft, writing – review and editing, visualization. Hugo Tavera: conceptualization, methodology, software. Frédérick Dallaire: methodology, formal analysis. Patrick Orsini: conceptualization, methodology, project administration. Keven Savard: conceptualization, methodology, visualization. Jacques Bismuth: conceptualization, methodology, software. Philippe Mckoy: conceptualization, methodology. Israel Veilleux: software, resources. Kevin Petrecca: supervision, project administration, funding acquisition, review & editing. Frédéric Leblond: supervision, project administration, funding acquisition, visualization, writing – review & editing.

Conflicts of interest

Kevin Petrecca and Frédéric Leblond are co-founders of Reveal Surgical, a medical device company that seeks to commercialize a Raman spectroscopy system for intraoperative cancer detection.

Acknowledgements

References

1 H. Dickhaus, K. Ganser, A. Staubert and M. Bonsanto, *Eng. Med. Biol. Soc.*, 1997, 0–3.

2 A. Nabavi, H. Thurm, B. Zountsas, T. Pietsch, H. Lanfermann, U. Pichlmeier and M. Mehdorn, *Neurosurgery*, 2009, **65**, 1070–1076.

3 L. Loh, P. Tiwari, J. Lee, O.-W. Low, V. Nallathamby, H. Lee, J. Lim, T. C. Lim and Y. L. Yap, *J. Skin Cancer*, 2021, **2021**, 4944570.

4 J. M. Laakman, S. J. Chen, K. S. Lake, J. L. Blau, D. A. Rajan, M. I. Samuelson and R. A. Robinson, *Am. J. Clin. Pathol.*, 2021, **156**, 461–470.

5 M. Diem, A. Mazur, K. Lenau, J. Schubert, B. Bird, M. Miljković, C. Krafft and J. Popp, *J. Biophotonics*, 2013, **6**, 855–886.

6 H. J. Byrne, M. Baranska, G. J. Puppels, N. Stone, B. Wood, K. M. Gough, P. Lasch, P. Heraud, J. Sulé-Suso and G. D. Sockalingum, *Analyst*, 2015, **140**, 2066–2073.

7 K. Hanna, E. Krzoska, A. M. Shaaban, D. Muirhead, R. Abu-Eid and V. Speirs, *Br. J. Cancer*, 2022, **126**, 1125–1139.

8 T. Hollon and D. A. Orringer, *J. Neurooncol.*, 2021, **151**, 393–402.

9 M. Jermyn, J. Mercier, K. Aubertin, J. Desroches, K. Urmey, J. Karamchandiani, E. Marple, M. C. Guiot, F. Leblond and K. Petrecca, *Cancer Res.*, 2017, **77**, 3942–3950.

10 J. Desroches, M. Jermyn, M. Pinto, F. Picot, M.-A. Tremblay, S. Obaid, E. Marple, K. Urmey, D. Trudel, G. Soulez, M.-C. Guiot, B. C. Wilson, K. Petrecca and F. Leblond, *Sci. Rep.*, 2018, **8**, 1792.

11 H. Noothalapati, K. Iwasaki and T. Yamamoto, *Spectrochim. Acta, Part A*, 2021, **258**, 119818.

12 H. Lui, J. Zhao, D. McLean and H. Zeng, *Cancer Res.*, 2012, **72**, 2491–2500.

13 J. Zhao, H. Zeng, S. Kalia and H. Lui, *Dermatol. Clin.*, 2017, **35**, 495–504.

14 I. P. Santos, R. van Doorn, P. J. Caspers, T. C. Bakker Schut, E. M. Barroso, T. E. C. Nijsten, V. Noordhoek Hegt, S. Koljenović and G. J. Puppels, *Br. J. Cancer*, 2018, **119**, 1339–1346.

15 F. Gaba, W. J. Tipping, M. Salji, K. Faulds, D. Graham and H. Y. Leung, *Cancers*, 2022, **14**(6), 1535.

16 M. Pinto, K. C. Zorn, J.-P. Tremblay, J. Desroches, F. Dallaire, K. Aubertin, E. T. Marple, C. Kent, F. Leblond, D. Trudel and F. Lesage, *J. Biomed. Opt.*, 2019, **24**, 1–10.

17 S. Tanwar, S. K. Paidi, R. Prasad, R. Pandey and I. Barman, *Spectrochim. Acta, Part A*, 2021, **260**, 119957.

18 A. N. Ramya, J. S. Arya, M. Madhukrishnan, S. Shamjith, M. S. Vidyalekshmi and K. K. Maiti, *Chem. – Asian J.*, 2021, **16**, 409–422.

19 I. P. Santos, E. M. Barroso, T. C. Bakker Schut, P. J. Caspers, C. G. F. van Lanschot, D.-H. Choi, M. F. van der Kamp, R. W. H. Smits, R. van Doorn, R. M. Verdijk, V. Noordhoek Hegt, J. H. von der Thüsen, C. H. M. van Deurzen, L. B. Koppert, G. J. L. H. van Leenders, P. C. Ewing-Graham, H. C. van Doorn, C. M. F. Dirven, M. B. Busstra, J. Hardillo, A. Sewnaik, I. ten Hove, H. Mast, D. A. Monserez, C. Meeuwis, T. Nijsten, E. B. Wolvius, R. J. Baatenburg de Jong, G. J. Puppels and S. Koljenović, *Analyst*, 2017, **142**, 3025–3047.

20 S. Hu, H. Kang, Y. Baek, G. El Fakhri, A. Kuang and H. S. Choi, *Adv. Healthcare Mater.*, 2018, **7**, 1800066.

21 D. DePaoli, É. Lemoine, K. Ember, M. Parent, M. Prud'homme, L. Cantin, K. Petrecca, F. Leblond and D. C. Côté, *J. Biomed. Opt.*, 2020, **25**, 1–36.

22 W. Stummer, U. Pichlmeier, T. Meinel, O. D. Wiestler, F. Zanella and H.-J. Reulen, *Lancet Oncol.*, 2006, **7**, 392–401.

23 B. W. Maloney, D. M. McLatchy III, B. W. Pogue, K. D. Paulsen, W. A. Wells and R. J. Barth, *J. Biomed. Opt.*, 2018, **23**, 100901.

24 E. Schmälzlin, B. Moralejo, I. Gersonde, J. Schleusener, M. E. Darvin, G. Thiede and M. M. Roth, *J. Biomed. Opt.*, 2018, **23**, 1–11.

25 E. M. Barroso, R. W. H. Smits, C. G. F. van Lanschot, P. J. Caspers, I. ten Hove, H. Mast, A. Sewnaik, J. A. Hardillo, C. A. Meeuwis, R. Verdijk, V. Noordhoek Hegt, R. J. Baatenburg de Jong, E. B. Wolvius, T. C. Bakker Schut, S. Koljenović and G. J. Puppels, *Cancer Res.*, 2016, **76**, 5945–5953.

26 F. Daoust, T. Nguyen, P. Orsini, J. Bismuth, M.-M. de Denus-Baillargeon, I. Veilleux, A. Wetter, P. McKoy, I. Dicaire, M. Massabki, K. Petrecca and F. Leblond, *J. Biomed. Opt.*, 2021, **26**, 1–18.

27 N. Yokoya, N. Miyamura and A. Iwasaki, *Appl. Opt.*, 2010, **49**, 4568–4575.

28 G. Sheehy, F. Picot, F. Dallaire, K. Ember, T. Nguyen, K. Petrecca, D. Trudel and F. Leblond, *J. Biomed. Opt.*, 2023, **28**, 25002.

29 D. T. Berhe, C. E. Eskildsen, R. Lametsch, M. S. Hviid, F. van den Berg and S. B. Engelsen, *Meat Sci.*, 2016, **111**, 18–26.

30 A. Beganović, L. M. Hawthorne, K. Bach and C. W. Huck, *Foods*, 2019, **8**, 49.

31 J. Platt, *Adv. Large Margin Classif.*, 1999, **10**, 61–74.

32 F. Pedregosa, G. Varoquaux, A. Gramfort, V. Michel, B. Thirion, O. Grisel, M. Blondel, P. Prettenhofer, R. Weiss, V. Dubourg, J. Vanderplas, A. Passos, D. Cournapeau, M. Brucher, M. Perrot and É. Duchesnay, *J. Mach. Learn. Res.*, 2011, **12**, 2825–2830.

33 American National Standards Institute, ANSI Z136.1: American National Standard for Safe Use of Lasers, 2014.

34 American National Standards Institute, ANSI Z136.3-2018 Safe Use Of Lasers In Health Care, 2018.

35 E. L. Jones, J. R. Oleson, L. R. Prosnitz, T. V. Samulski, Z. Vujaskovic, D. Yu, L. L. Sanders and M. W. Dewhirst, *J. Clin. Oncol.*, 2005, **23**, 3079–3085.

36 N. R. Datta, D. Marder, S. Datta, A. Meister, E. Puric, E. Stutz, S. Rogers, B. Eberle, O. Timm, M. Staruch, O. Riesterer and S. Bodis, *Int. J. Hyperthermia*, 2021, **38**, 296–307.

37 R. M. Jones, S. Kamps, Y. Huang, N. Scantlebury, N. Lipsman, M. L. Schwartz and K. Hynynen, *J. Neurosurg.*, 2020, **132**, 1802–1809.

38 S. A. Sapareto and W. C. Dewey, *Int. J. Radiat. Oncol., Biol., Phys.*, 1984, **10**, 787–800.

39 A. B. Harris, L. Erickson, J. H. Kendig, S. Mingrino and S. Goldring, *J. Neurosurg.*, 1962, **19**, 514–521.

40 G. C. van Rhoon, T. Samaras, P. S. Yarmolenko, M. W. Dewhirst, E. Neufeld and N. Kuster, *Eur. Radiol.*, 2013, **23**, 2215–2227.

41 N. Bosschaart, G. J. Edelman, M. C. G. Aalders, T. G. Van Leeuwen and D. J. Faber, *Lasers Med. Sci.*, 2014, **29**, 453–479.

42 R. Matika, M. Ibrahim and A. Patwardhan, *Temperature*, 2017, **4**, 9–12.

43 M. A. Ansari, M. Erfanzadeh and E. Mohajerani, *J. Lasers Med. Sci.*, 2013, **4**, 99–106.

44 A. Das, A. Sarda and A. De, *J. Cutan. Aesthet. Surg.*, 2016, **9**, 215–219.